



HAL
open science

Modal characterization of crack network development in an MgO containing refractory castable

Vinicius Fiocco Sciuti, Rafael Vargas, Rodrigo Bresciani Canto, François Hild

► To cite this version:

Vinicius Fiocco Sciuti, Rafael Vargas, Rodrigo Bresciani Canto, François Hild. Modal characterization of crack network development in an MgO containing refractory castable. *Journal of Strain Analysis for Engineering Design*, 2023, 58 (6), pp.490-500. 10.1177/03093247221141490 . hal-03956964

HAL Id: hal-03956964

<https://hal.science/hal-03956964v1>

Submitted on 25 Jan 2023

HAL is a multi-disciplinary open access archive for the deposit and dissemination of scientific research documents, whether they are published or not. The documents may come from teaching and research institutions in France or abroad, or from public or private research centers.

L'archive ouverte pluridisciplinaire **HAL**, est destinée au dépôt et à la diffusion de documents scientifiques de niveau recherche, publiés ou non, émanant des établissements d'enseignement et de recherche français ou étrangers, des laboratoires publics ou privés.



Distributed under a Creative Commons Attribution - NonCommercial 4.0 International License

Modal characterization of crack network development in an MgO containing refractory castable

The Journal of Strain Analysis for
Engineering Design
0(0):1–10
©The Author(s) 2021
Reprints and permission:
sagepub.co.uk/journalsPermissions.nav
DOI: 10.1177/03093247221141490
www.sagepub.com/

SAGE

Vinicius Fiocco Sciuti^{1,2}, Rafael Vargas^{1,3}, Rodrigo Bresciani Canto^{1,2} and François Hild³

Abstract

Damage due to MgO hydration in castables has been studied by bar resonance and recently by Digital Image Correlation (DIC). The hydration reaction kinetics was studied via principal component analyses (PCA) applied to DIC results of images acquired during 60 h of curing and drying of an MgO containing refractory castable. The experiment was carried out in a in-house climatic chamber at 50 °C and 50% of relative air humidity. The displacement and maximum eigen strain fields were obtained via DIC. Their PCA revealed the crack network as the most relevant component, with a temporal development of a sigmoidal curve where a two-parameter Weibull law was satisfactorily fitted. The reaction duration was virtually identical for both fields, and only a time shift in reaction initiation and saturation was attributed to the choice of field. The approach allows the need for user-defined thresholds to be avoided for crack quantification.

Keywords

Curing and drying, Digital Image Correlation (DIC), Principal Component Analysis (PCA), Reaction kinetics, Crack network

Introduction

High alumina refractory castables containing magnesia (MgO) are interesting for industry due to many advantages, mainly related to *in situ* spinel (MgAl_2O_4) formation¹. However, MgO hydrates during curing and drying of such castables generating brucite ($\text{Mg}(\text{OH})_2$)^{2,3}, which in excess may damage the material^{4,5}. Many techniques have been used to study damage inception and growth (*e.g.*, TGA⁶, diametral compression (Brazilian test)⁴, and Bar Resonance⁷). Digital Image Correlation (DIC) was also applied for damage quantification⁸. Sciuti *et al.*⁹ designed a climatic chamber to capture *in situ* images of cubic specimens during curing and drying. The crack network was evaluated by assessing the surface crack density and Mean Crack Opening Displacement (MCO) fields on the surface of the specimen. The MCO was obtained from the product of the maximum eigen strain of any given element by its length. The authors demonstrated via tomographic scans that the cracks initiated on the surface and propagated toward the center.

In the present study, it is proposed to analyze damage growth in one of such tests via Principal Component Analyses (PCAs). In PCAs, truncated bases of separated modes are constructed¹⁰. In the sequel, PCA is based on the singular value decomposition (SVD¹¹) of measured displacement and strain fields via DIC. For instance, SVD was used in modal analyses of dynamic systems¹² and for image denoising¹³. Trebuna *et al.*¹⁴ applied SVDs to displacements measured via stereo-DIC to find vibrational modes of a piece of paper in front of a speaker. The authors showed a potential methodology to study dynamic systems via DIC and two fast cameras. A deflectometry setup assembled with a single standard camera was used to

measure the first eight modes of a vibrating cantilever plate¹⁵ whose apparent deformation was measured via global DIC, and the strain field was post-processed via PCA.

Gramma and Subramanian¹⁶ applied PCAs to horizontal and vertical displacement fields to compute the strain fields from DIC results using synthesized pairs of images to recreate different analytical cases. They proposed the PCA as a tool to reduce dimensionality of the displacement data and mitigate noise. The effectiveness of PCA on noise reduction for DIC displacement fields was also evaluated by Hao *et al.*¹⁷. The authors used PCA to reduce spurious fluctuations in high-temperature DIC results. The procedure was applied to displacement fields for a synthetic set of images and another using images from a tensile test at high temperature. The displacement fields obtained directly by DIC were compared to the other obtained after the PCA procedure, whose effectiveness was proven.

Spacetime DIC registrations of infrared images were conducted with a reduced set of modes constructed via numerical thermomechanical simulations of laser shocks on stainless steel plate¹⁸. The previous model order

¹Federal University of São Carlos, Graduate Program in Materials Science and Engineering (PPGCEM), 13565-905, São Carlos-SP, Brazil

²Federal University of São Carlos (UFSCar), Department of Materials Engineering (DEMa), 13565-905, São Carlos-SP, Brazil

³Université Paris-Saclay, CentraleSupélec, ENS Paris-Saclay, CNRS, LMPS - Laboratoire de Mécanique Paris-Saclay, 91190 Gif-sur-Yvette, France

Corresponding author:

Vinicius Fiocco Sciuti, Federal University of São Carlos (UFSCar), Department of Materials Engineering (DEMa) São Carlos, São Paulo, 13565-905, Brazil.

Email: vinicius.sciuti@ufscar.br

reductions were performed a posteriori to extract meaningful modes. An alternative route consists in performing such procedures on the fly. They correspond to Proper Generalized Decompositions (PGD). Passieux and Périé¹⁹ introduced a new approach to DIC procedure based on PGD in which spatial modes were separated. Berny *et al.*²⁰ used PGD-DIC in a space/time separation to capture displacement fields of a dynamic Brazilian test on Ductal concrete.

This work aims to demonstrate that PCA applied to DIC results can provide more information than the well-known denoising effect. Obtaining the spatial and the temporal modes makes it possible to follow the kinetics of a damaging hydration reaction by means of kinematic analyses. The most interesting contribution is that the information about the crack network development is provided by an algebraic procedure, the PCA, and no inferences are made about what should be considered a crack or not. The case study deals with a cubic specimen made of a refractory castable containing magnesia (MgO), which generates brucite ($\text{Mg}(\text{OH})_2$) during hydration.

The analyses focus on the investigation of the crack network, and they are divided into two approaches. First, PCA is applied to measured displacement fields and the effect of the rigid body motions on the temporal modes is discussed. The maximum eigen strain fields are also studied within the present framework. The truncation error evaluates the loss of information caused by using a subgroup of modes to reconstruct a given field. One new key ingredient in the analyses is the truncation error related to measurement uncertainties. The first spatial mode shows that the crack opening field is the most relevant cause of displacement when the fluctuations due to rigid body motions are discarded. The first temporal mode is used to follow the kinetics of the underlying reaction.

Material and Methods

Material and Specimen Production

The studied material is a high alumina refractory castable containing 6 wt.% of caustic magnesia (98 wt.% MgO $d_{90} < 33 \mu\text{m}$ RHI Magnesita, Brazil) and high specific surface area ($24.6 \text{ m}^2\text{g}^{-1}$). The detailed composition is presented in Ref.⁹. The material was prepared in a castable rheometer, and the resulting mix was cast under vibration into silicone molds of size $70 \times 70 \times 70 \text{ mm}^3$ to produce cubic specimens (Figure 1(a)). The edge size of the cube (70 mm) was selected to be over ten times the average diameter of the largest aggregates ($\approx 6 \text{ mm}$). The specimens were demolded after three hours at $50 \text{ }^\circ\text{C}$ and 50% relative air humidity. The sample face of interest was speckled with black paint to provide a wide variety of gray levels for the DIC procedure as the castable surface had a light and mat hue. The considered ROI is shown in Figure 1.

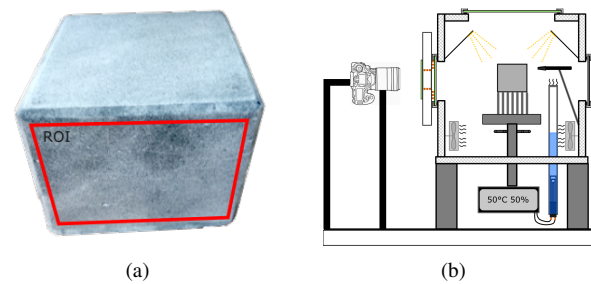


Figure 1. (a) Fabricated specimen and (b) climatic chamber used in the experiment to allow for image acquisition. The Region of Interest (ROI) used in the DIC analyses is marked in red (ROI size $\approx 60 \times 60 \text{ mm}^2$). Adapted from⁹

The specimen was kept inside a climatic chamber at $50 \text{ }^\circ\text{C}$ and 50 % of relative air humidity, with transparent glass windows that were used to acquire images during its curing and drying (Figure 1(b)). More details about the climatic chamber are given in Ref.⁹ The hardware parameters of the optical setup are reported in Table 1

Table 1. DIC hardware parameters

Camera	CANON T5 Rebel
Definition	3529 × 5296 pixels (Bayer pixels)
Color filter	Bayer
Gray Levels amplitude	16 bits
Lens	CANON 100-mm macro
Aperture	$f/22$
Field of view	$65 \times 65 \text{ mm}^2$
Image scale	$50 \mu\text{m} / \text{pixel}$
Stand-off distance	102 cm
Image acquisition rate	6 fpmin ^b and 2 fph [‡]
Exposure time	3.2 s
Patterning technique	sprayed black paint
Pattern feature size [‡]	4 pixels (B/W)

^bten images used to evaluate measurement uncertainties

[‡]images of the crack network

[‡]evaluated as full width at half maximum of autocorrelation function

PCA Procedure

DIC analyses were carried out using the Correli 3.0 framework²¹ (Table 2). A structured mesh made of 3-noded triangles (of size $\approx 5 \text{ px}$) was constructed. FE-DIC was run with a regularization length of 10 px. Ten images were acquired at the beginning of the experiment, before the initiation of cracks. This set was used to quantify the uncertainty of displacement and strain field measurements due to experimental artifacts such as the quality of the speckle and changes in lighting caused by the vapor stream inside the chamber. Most of the gray level variations were corrected using brightness and contrast corrections²². The output of such analyses is a series of m nodal displacements gathered in a column vector $\{\mathbf{u}^i\}$ for any analyzed picture $i = 1, \dots, n$. All these column vectors are gathered in a rectangular matrix $[\mathbf{U}]$ (of dimension $m \times n$) that corresponds to a space/time separation of the measured data.

Table 2. DIC analysis parameters

DIC software	Correli 3.0 ²¹
Image filtering	none
Shape functions	linear (T3)
Element length	5 px
Matching criterion	regularized sum of squared differences
Interpolant	cubic
Strain calculation	derivative of shape functions
Regularization length	10 px

SVD deals with rectangular matrices $[\mathbf{U}]_{m \times n}$, with $m > n$ in the present case. The product $[\mathbf{U}][\mathbf{U}]^T$ is considered to obtain a square matrix, and then its eigen decomposition

$$p(\lambda) = \det([\mathbf{U}][\mathbf{U}]^T - \lambda[\mathbf{I}]) = 0, \quad (1)$$

is carried out to determine the eigen values λ from the characteristic polynomial p . This decomposition provides so-called singular values that are the square root of the previous eigen values ($s_i = \sqrt{\lambda_i}$). SVD results in three matrices, namely, the singular values $[\mathbf{S}]_{m \times n}$, and the modal matrices $[\mathbf{V}]_{m \times m}$ and $[\mathbf{T}]_{n \times n}$, which permit the matrix $[\mathbf{U}]$ to be recovered,

$$[\mathbf{U}] = [\mathbf{V}][\mathbf{S}][\mathbf{T}]^T, \quad (2)$$

where $[\mathbf{S}]$ is a diagonal matrix with the singular values s_i ordered by importance ($s_1 \geq s_2 \geq s_3 \geq \dots s_n$). Associated with the space/time separation, the matrix $[\mathbf{V}]$ is composed of spatial modes (SM), whereas the matrix $[\mathbf{T}]$ contains the temporal modes (TM).

Figure 2 illustrates the procedure for a hypothetical mesh with 16 nodes and five pictures (Figure 2(a)). The nodal values distributed for a 4×4 matrix are vectorized into a 16×1 column vector. This procedure is repeated for each picture, and the column vectors are stacked to create matrix $[\mathbf{U}]$ (Figure 2(b)). The SVD generates matrices $[\mathbf{S}]$, $[\mathbf{T}]$, and $[\mathbf{V}]$ (Figure 2(c)). Each $[\mathbf{V}]$ column corresponds to a spatial mode (SM), which is reshaped back as a 4×4 matrix to be consistent with the original mesh (as shown in Figures 7, and 9). The columns of $[\mathbf{T}]$ correspond to the temporal modes (TM), which may be graphically represented vs. time (see Figures 3, 4, 6, and 8).

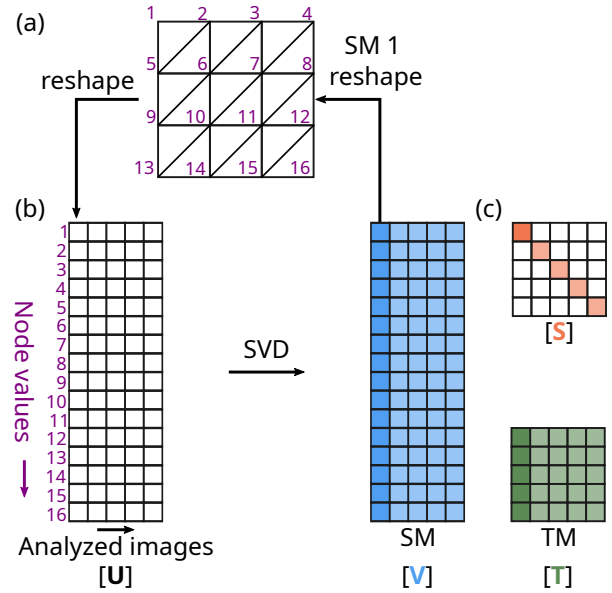


Figure 2. (a) Illustration of the SVD procedure for a hypothetical mesh with 16 nodes. (b) The SVD procedure generates the singular values $[\mathbf{S}]$, the SMs $[\mathbf{V}]$, and the TMs $[\mathbf{T}]$ (c). Each SM is a column of matrix $[\mathbf{V}]$ that is reshaped to fit the original mesh

In the following analyses, SVD was carried out using the algorithm implemented in Matlab (*i.e.*, $[\mathbf{V}, \mathbf{S}, \mathbf{T}] = \text{svd}(\mathbf{U}, 'econ')$ *). The studied case consists of a mesh with 40,000 nodes (with two DOFs per node) and 200 images were analyzed. Therefore, an $80,000 \times 200$ $[\mathbf{U}]$ matrix was created.

The SVD written in Equation (2) is complete and exact. The $[\mathbf{S}]$ matrix gathers its eigenvalues, and it is a direct indicator that some modes are orders of magnitude more relevant than others because of their ranking. The proposed decomposition is used for the Principal Component Analysis (PCA), by truncating $[\mathbf{U}]$ to obtain the approximation $[\mathbf{U}_k]$ with the first k modes

$$[\mathbf{U}_k] = [\mathbf{V}_k][\mathbf{S}_k][\mathbf{T}_k]^T, \quad (3)$$

where $[\mathbf{S}_k]$ contains the first k singular values (*i.e.*, diagonal matrix of dimension $k \times k$), and $[\mathbf{V}_k]$ and $[\mathbf{T}_k]$ are the corresponding reduced modal matrices of dimension $m \times k$ and $n \times k$, respectively. In the following analyses, the truncation error will be compared to the uncertainty level of the considered quantity.

The same type of decomposition and reduction are to be applied to strain data that are also separated in space and time to form rectangular matrices $[\mathbf{E}]_{p \times n}$, where p is the number of elements. In the present case, $p = 79,202$ elements were considered and maximum eigen strain ϵ_1 fields were selected to monitor the development of damage^{8,9}. It is worth noting that the strains are uniform over each element, and only one value was kept for each element. The interest of considering strain fields in addition to displacement fields is that they are insensitive to rigid body motions. This particular point is addressed hereafter.

*A considerable amount of RAM may be needed depending on the mesh size and number of frames. By using the 'econ' option, very similar results are obtained using less resources.

Results and Discussion

PCA applied to Measured Fields

The spectrum of singular values normalized by the highest one (*i.e.*, s_1) are shown in Figure 3(a). It is observed that s_1 is more than 10 times greater than s_2 , which indicates that mode 1 (*i.e.*, TM1 and SM1) may be sufficient for the reconstruction of the displacement field. TMs 1, 2 and 3 are reported in Figure 3(b). Because of very high fluctuations, no clear temporal signature is observed.

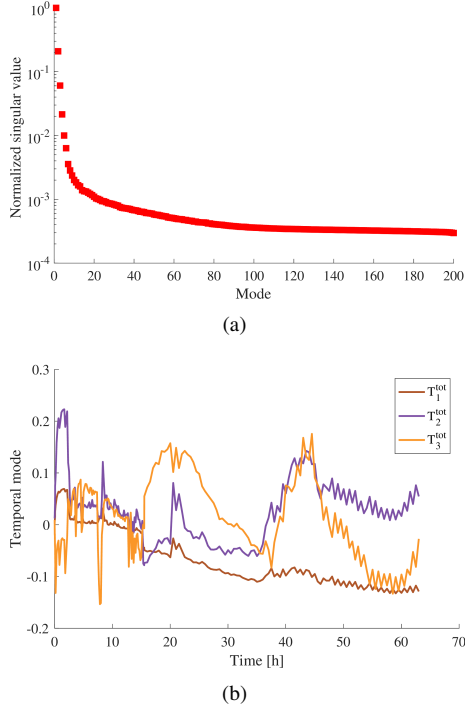


Figure 3. Singular values (a) and first three temporal modes (b) for \mathbf{u}^{tot}

Searching for the source of these fluctuations, the displacement fields provided by DIC (*i.e.*, \mathbf{u}^{tot}) were split into rigid body motions \mathbf{u}^{rbm} and the part that causes deformation, called mechanical displacement \mathbf{u}^{mec}

$$\mathbf{u}^{\text{tot}}(\mathbf{x}, t) = \mathbf{u}^{\text{rbm}}(\mathbf{x}, t) + \mathbf{u}^{\text{mec}}(\mathbf{x}, t) \quad (4)$$

From the measured displacement fields $\mathbf{u}^{\text{tot}}(\mathbf{x}, t)$, the three rigid body contributions (*i.e.*, translation along x and y , and rotation about z) were determined via least squares fit for each frame independently. The measured nodal displacements were projected onto a reduced basis consisting of two (unitary and orthogonal) translations and one rotation field about the center of the ROI. The field \mathbf{u}^{mec} then corresponds to the residual $\mathbf{u}^{\text{mec}}(\mathbf{x}, t) = \mathbf{u}^{\text{tot}}(\mathbf{x}, t) - \mathbf{u}^{\text{rbm}}(\mathbf{x}, t)$. The SVD procedure was applied to each part of \mathbf{u}^{tot} . The corresponding normalized singular values and TMs are shown in Figure 4 for \mathbf{u}^{rbm} . It is interesting to note that the first three singular values associated with \mathbf{u}^{rbm} are very high (*i.e.*, more than ten orders of magnitude) in comparison with all other ones (Figure 4(a)). This difference is to be expected for such field that consists of three components and then measurement uncertainties. The temporal fluctuations of the first three TMs are similar for \mathbf{u}^{rbm} (Figure 4(b)) and \mathbf{u}^{tot} (Figure 3(b)).

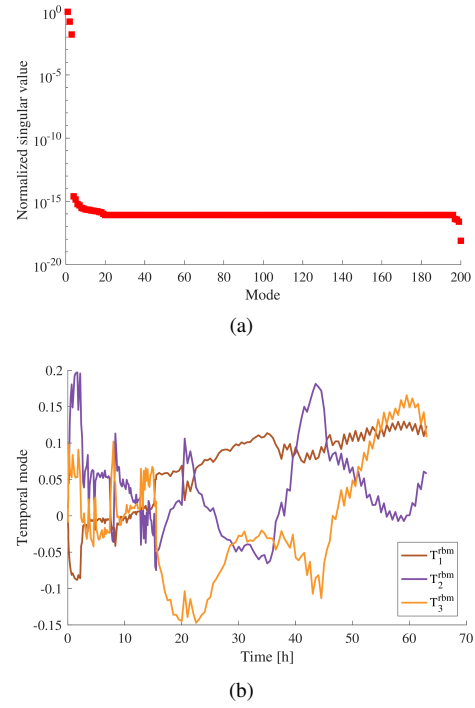


Figure 4. Singular values (a) and first three temporal modes (b) for \mathbf{u}^{rbm}

Even though rigid body motions can be described by one vertical and one horizontal translation combined with one rotation field as previously described, the SVD of \mathbf{u}^{rbm} provides orthogonal modes that are linear combinations of those fields that were used to calculate \mathbf{u}^{rbm} . This observation is confirmed in Figure 5.

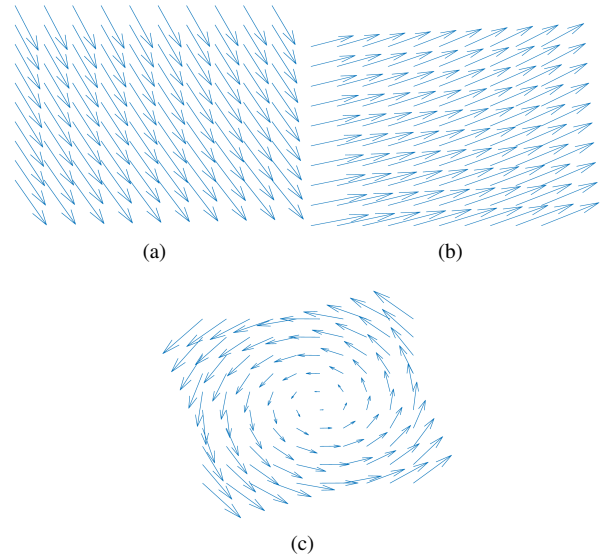


Figure 5. First (a), second (b) and third (c) spatial modes for \mathbf{u}^{rbm}

Figure 6(a) shows that for \mathbf{u}^{mec} the first eigen value is very high in comparison to the next ones. This difference was not as high for \mathbf{u}^{tot} (Figure 3(a)). Further, smoother changes are observed for the first two TMs (Figure 6(b)) in comparison to the previous ones (Figures 3(b) and 4(b)).

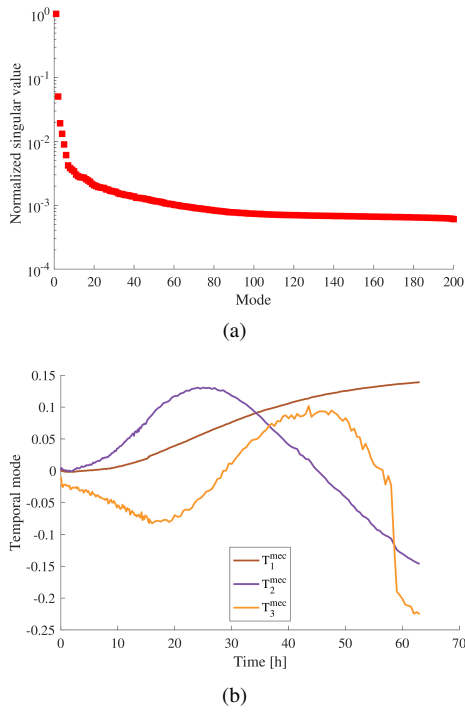


Figure 6. Singular values (a) and first three TMs (b) for \mathbf{u}^{mec}

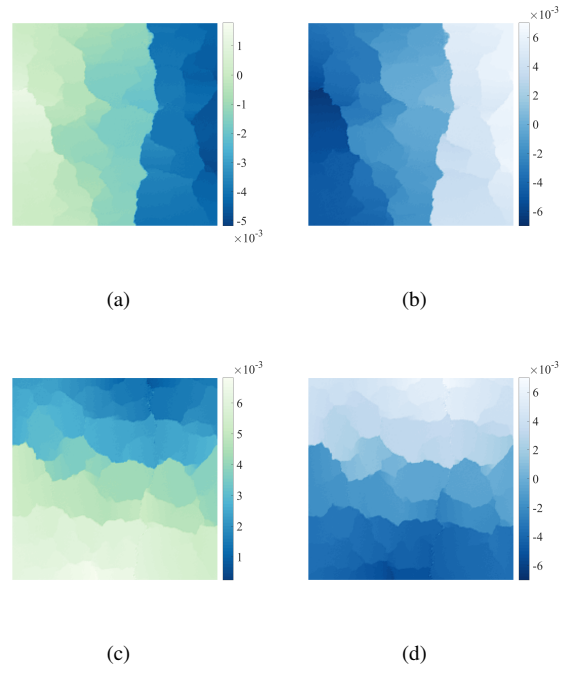


Figure 7. First spatial mode for \mathbf{u}^{tot} (a,c) and \mathbf{u}^{mec} (b,d) in the horizontal (a,b) and vertical (c,d) directions

The SVD procedure was also applied to the maximum eigen strain ϵ_1 field by constructing the matrix $[\mathbf{E}]$ as explained above.

The singular values and the first three TMs for ϵ_1 are shown in Figure 8. The first singular value is five times higher than the second one, thereby indicating a good separation between them. The TMs shown in Figure 8 (b) are rather smooth and similar to those of \mathbf{u}^{mec} , except for the (arbitrary) sign.

The first spatial modes of \mathbf{u}^{tot} and \mathbf{u}^{mec} are shown in Figure 7, which are interpreted as the mapping of ROI sub-regions according to the most relevant displacements. The limits of each sub-region in the SMs appear as abrupt changes in displacements, which indicate the complexity of the crack network. Since they are the first SM for \mathbf{u}^{tot} and \mathbf{u}^{mec} , the displacements caused by the development of cracks are dominant. The crack network is visible in the first SM of \mathbf{u}^{tot} in addition to rigid body motions. The TMs were significantly different for the two fields. Another consequence of measurement uncertainty is the grainy hues in the sub-regions of \mathbf{u}^{tot} SM when compared to the smoother hues for \mathbf{u}^{mec} . This is an additional reason for focusing the study on \mathbf{u}^{mec} .

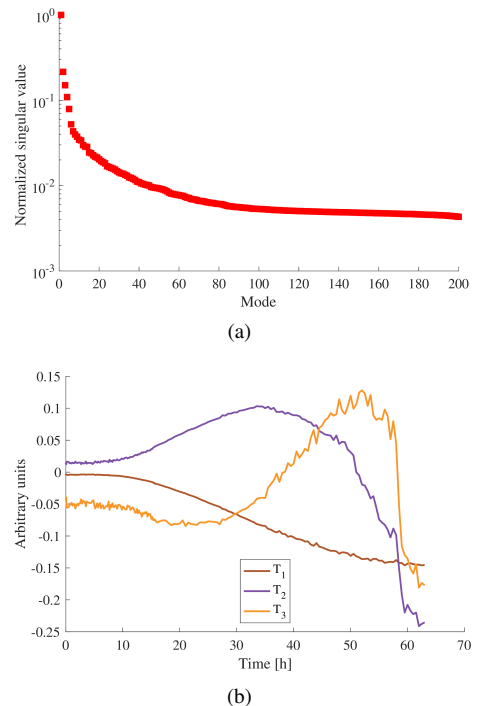


Figure 8. Singular values (a) and first three TMs (b) for ϵ_1

The first three SMs are shown in Figure 9 for ϵ_1 . The crack network is apparent in all three SMs, mainly in the first one, confirming that crack openings are the main event of the displacements on the surface of the specimen. The second and third SMs separate the cracks into two groups. It is worth noting that the first SM has levels essentially in the contraction regime (*i.e.*, $\epsilon_1 < 0$). This trend is to be expected since the first TM was negative so that their product becomes positive, which is expected for mode I cracks.

The previous discussion focused on the first three modes in an arbitrary way. In the following analyses, the measurement uncertainties are evaluated and will be used in the truncation of Equation (2).

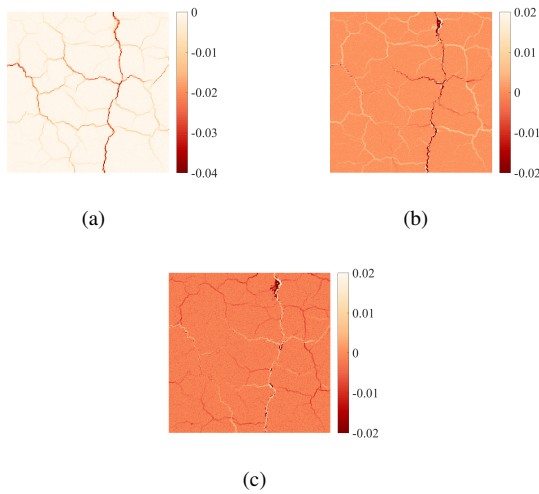


Figure 9. First (a), second (b), and third (c) spatial modes of the maximum eigen strain field

Truncation Based on Uncertainties

The 10 initial images were used to evaluate the measurement uncertainties. For this analysis, each independent image pair was used, thereby resulting in a set of 90 DIC results for displacement and strain fields. The variance was computed time-wise for each degree of freedom of the displacement fields \mathbf{u}^{tot} , \mathbf{u}^{rbm} and \mathbf{u}^{mec} . Figure 10 shows the standard uncertainty fields for all three fields. Some areas with high uncertainties are observed in Figure 10(a,c,d,f) due to open pores on the castable surface. Such features create shadow regions that result in low gray level gradients, which increase the uncertainty levels. The spots with higher uncertainty in Figure 10(c) are due to the effect of pores. The same spots are less visible in Figure 10(a) because of the high fluctuations associated with rigid body motions, which are higher than those for mechanical displacements. The same phenomenon is observed for the vertical component (Figure 10(d-f)). However, the fluctuations of \mathbf{u}^{rbm} are higher in the vertical direction (Figure 10(e)) than in the horizontal one (Figure 10(b)), and the gradient of these fields indicates the presence of a rotation. It may be caused by an accommodation of the specimen on the metal rods of the specimen support (Figure 1) that may slightly move and bend (*i.e.*, fulfilling their intended role).

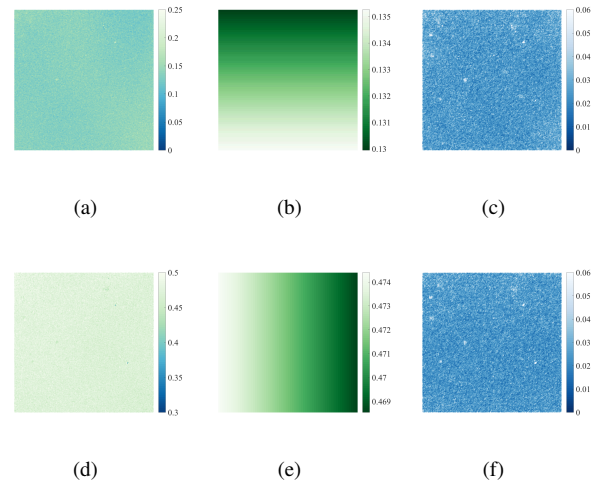


Figure 10. Standard displacement uncertainty fields for \mathbf{u}^{tot} (a,d), \mathbf{u}^{rbm} (b,e), and \mathbf{u}^{mec} (c,f) in the horizontal (a-c) and vertical (d-f) directions. The displacements are expressed in pixels

Table 3 shows the standard displacement uncertainties computed as the root mean of the variance fields for each direction. For \mathbf{u}^{rbm} , the levels are one order of magnitude higher than those of \mathbf{u}^{mec} , and close to those of \mathbf{u}^{tot} . This result indicates that the temporal fluctuations due to \mathbf{u}^{rbm} cause most of those of \mathbf{u}^{tot} . The rather low fluctuations of \mathbf{u}^{mec} are closer to measurement uncertainties expected from DIC measurements²³.

Table 3. Standard displacement uncertainties (expressed in px) for the three considered fields

	\mathbf{u}^{tot}	\mathbf{u}^{rbm}	\mathbf{u}^{mec}
x	0.14	0.13	0.03
y	0.47	0.47	0.03

The same analysis was carried out for the maximum eigen strain field computed from \mathbf{u}^{tot} (or equivalently from \mathbf{u}^{mec}) whose uncertainty field is shown in Figure 11. A rather uniform distribution is observed. The corresponding standard strain uncertainty is equal to 0.53%.

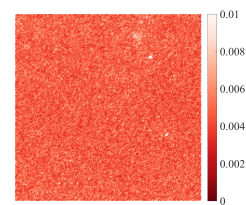


Figure 11. Standard uncertainty field for the maximum eigen strain ϵ_1

The Signal to Noise Ratio (SNR) is introduced as an indicator for the truncation error. First, the standard deviation of the truncation error was estimated for various numbers of modes. Then it was divided by the standard displacement uncertainty (Table 3). Figure 12 shows the change of SNR of the truncation error for the three considered displacement

fields and for the maximum eigen strains. The horizontal line $\text{SNR} = 1$ shows the limit at which the truncation error reaches the measurement uncertainty. In the present case, using two terms for \mathbf{u}^{tot} , one term for \mathbf{u}^{rbm} and 7 for \mathbf{u}^{mec} would be the optimal truncation. If only one mode was kept, the truncation error is about three times the measurement uncertainty, which is already very low.

The optimal truncation for ϵ_1 uses 14 terms as shown in Figure 12(b) with a smoother decay. For comparison, the truncation of \mathbf{u}^{mec} had only one term above twice the uncertainty level ($\text{SNR} > 2$) and ϵ_1 has only two terms (the second being 2.09). If only one mode is kept, the truncation error is less than three times the measurement uncertainty, which is again very low.

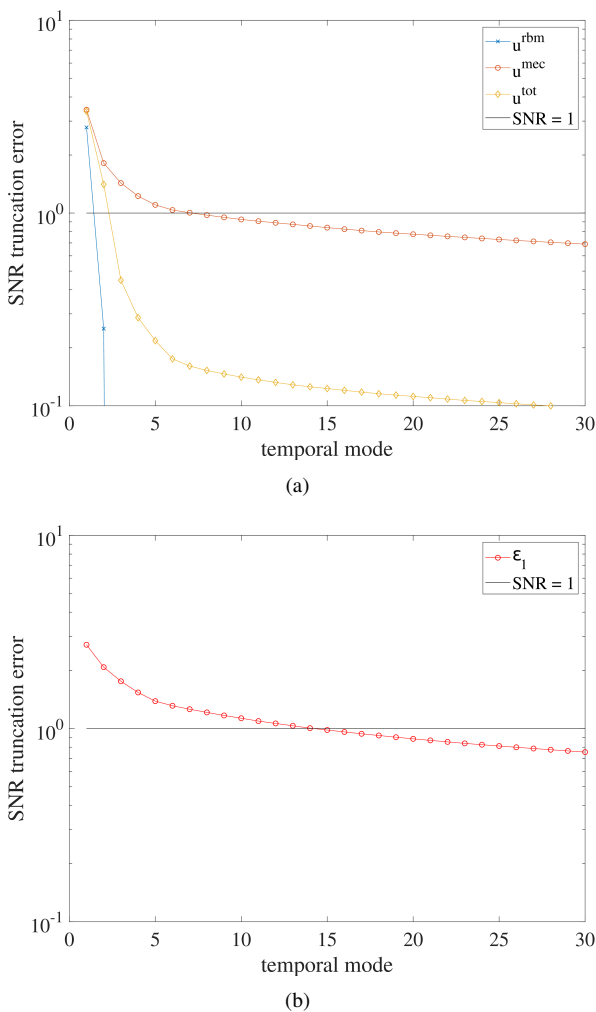


Figure 12. Truncation errors as functions of number of modes for (a) \mathbf{u}^{tot} , \mathbf{u}^{rbm} , \mathbf{u}^{mec} , and (b) ϵ_1

From all these analyses, it is concluded that the truncation to the the first mode of \mathbf{u}^{mec} and the maximum eigen strain field provides most of the experimental information with a big order reduction.

Curing and Drying Kinetics

The following analyses deal with the first mode of the displacement and strain fields

$$[\mathbf{U}_1^{\text{mec}}] = s_1^{\text{mec}} \{ \mathbf{V}_1^{\text{mec}} \} \{ \mathbf{T}_1^{\text{mec}} \}^{\top}$$

and (5)

$$[\mathbf{E}_1] = s_1 \{ \mathbf{V}_1 \} \{ \mathbf{T}_1 \}^{\top}$$

The MCOD fields are obtained from the maximum eigen strain field⁹ associated with $[\mathbf{U}_1^{\text{mec}}]$, $[\mathbf{E}_1]$, and from raw DIC (*i.e.*, without PCA). The study focuses on $t = 24$ h after the beginning of the experiment because the crack network is well developed but the MCOD values are not very high to hide the uncertainties in the aggregate cluster regions.

The MCOD fields reported in Figure 13(a,c,e) are virtually the same for all three types of analyses, showing that the crack network is well represented by the first mode of both fields. There is a grainy texture between cracks (Figure 13(e,f)) caused by measurement uncertainties. These grainy regions are not present in Figure 13(a-d) because of filtering attributed to PCA^{17,18}.

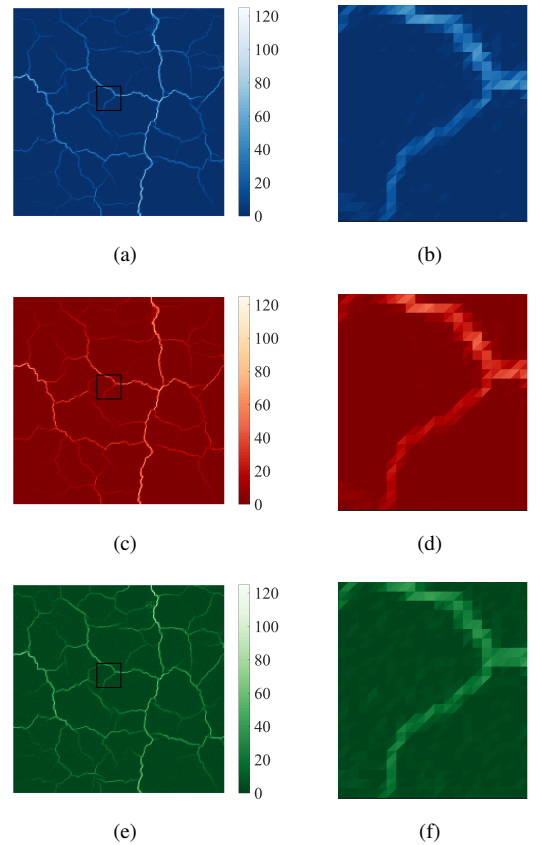


Figure 13. Mean crack opening displacement (expressed in μm) fields computed from $[\mathbf{U}_1^{\text{mec}}]$ (a), $[\mathbf{E}_1]$ (c), and derived from the measured displacement field via raw DIC (e) when $t = 24$ h. The details corresponding to the black box are shown in sub-figures (b,d,f)

For further comparison, the MCOD histograms of the previous fields are shown in Figure 14. The denoising effect of PCA is represented by a predominance of $[\mathbf{U}_1^{\text{mec}}]$ and $[\mathbf{E}_1]$ MCOD close to zero, while MCODs derived from

raw DIC have a higher number of elements from 5 to about 40 μm , when compared to the other ones (note the logarithmic scale), which is associated with measurement uncertainties due to humidity effects inside the climatic chamber.

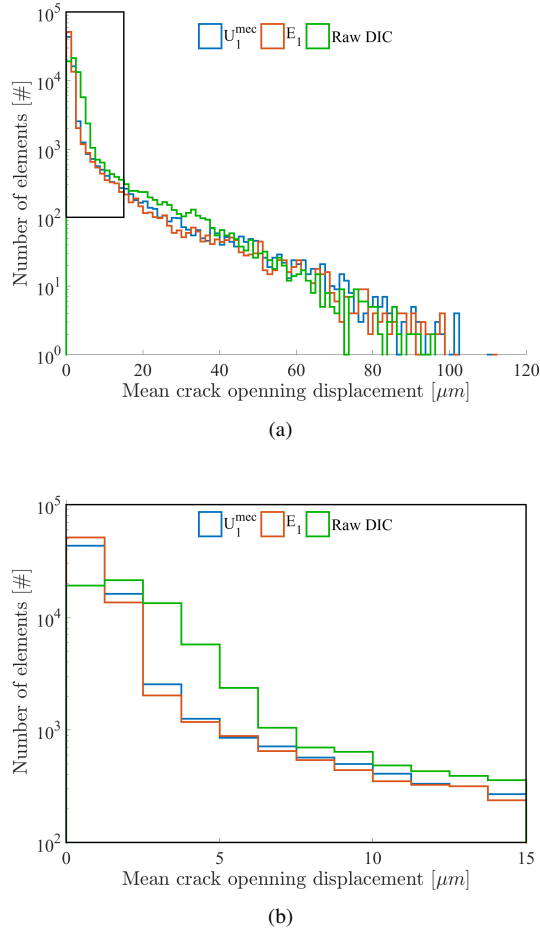


Figure 14. (a) Histograms of mean crack opening displacement computed from $[U_1^{\text{mec}}]$, $[E_1]$, and the raw DIC result ϵ_1 when $t = 24$ h. (b) Corresponding detail for lower CMOD levels corresponding to the black box shown in sub-figure (a)

The first TMs are approximated with the two-parameter Weibull law^{24,25}

$$T_1(t) = T_\infty \left(1 - \exp \left(- \left(\frac{t}{t_c} \right)^m \right) \right) \quad (6)$$

where m is the shape parameter (or Weibull modulus), t_c the scale parameter, and T_∞ a normalizing constant. In the present case, t_c defines the characteristic time of the studied transformation, namely, all durations to be introduced are proportional to t_c . The incubation time t_i is defined for a conventional transformation probability P . Similarly, the saturation time t_s is defined with $1 - P$ so that the damage duration becomes $\Delta t_d = t_s - t_i$

$$\begin{aligned} \frac{t_i}{t_c} &= (-\log(1 - P))^{1/m} \\ \frac{t_s}{t_c} &= (-\log(P))^{1/m} \\ \frac{\Delta t_d}{t_c} &= \left((-\log(P))^{1/m} - (-\log(1 - P))^{1/m} \right) \end{aligned} \quad (7)$$

The parameters m and t_c were obtained via least squares fit of the TMs. Figure 15(a) shows that the proposed fit

is in good agreement with experimental observations. The value $P = 5\%$ was chosen to avoid fluctuations on extremes of the TMs (Figure 15(b)).

Table 4 gathers the Weibull parameters and the corresponding duration Δt_d . The latter is very close for both ways of expressing the first TM, namely, via u^{mec} or ϵ_1 even though the characteristic time and Weibull modulus are different. In the present case, the first kinematic mode is related to the development of the crack network, which is caused by the excess of MgO hydration during the curing and drying of the castable. The hydration kinetics is followed by means of damage evaluations⁹. The parameter Δt_d characterizes the duration of damage growth (due to the underlying reaction).

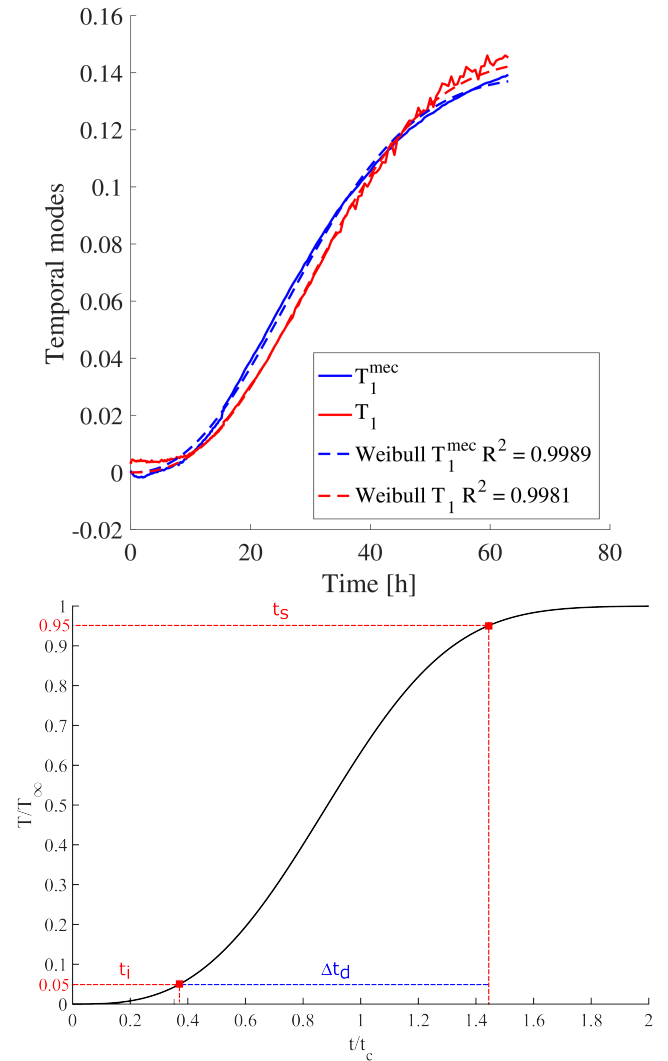


Figure 15. (a) First TMs associated with u^{mec} and ϵ_1 and their Weibull fit, (b) depiction of the incubation and saturation times, as well as damage duration when $P = 5\%$.

The damage duration Δt_d is close when using u^{mec} or ϵ_1 (Table 4), which is very important for the kinetic characterization of the studied process. If Δt_d had varied with the analyzed field, it would mean that there existed an interference of the PCA procedure in the kinetics, which may be an apparent acceleration (*i.e.*, reduced Δt_d) or retardation (*i.e.*, increase in Δt_d).

Table 4. Weibull parameters and corresponding durations for the first TM associated with \mathbf{u}^{mec} and ϵ_1

Analyzed field	m	t_c [h]	Δt_d [h]	t_i [h]	t_s [h]
\mathbf{u}^{mec}	2.3	33.7	45.6	9.1	54.7
ϵ_1	2.6	36.9	44.0	12.0	56.0

Conclusion

The curing and drying of a MgO containing refractory castable was carried out in a climatic chamber with windows for image acquisition. Digital images of one face of a cubic specimen were acquired for 60 h to monitor the development of the crack network via DIC. Principal Component Analyses (PCAs) were applied to DIC results such as the so-called mechanical displacement field (\mathbf{u}^{mec}) and the maximum eigen strain field (ϵ_1). The goals of the procedure were: i) denoise the DIC results, ii) prove that the most relevant displacements (or strains) are caused by the crack network development, and iii) quantify the MgO hydration kinetics by means of possibly one temporal mode.

By applying PCAs to the displacement fields, it was found that the rigid body motions were one source of fluctuations, which call for the procedure to be applied to \mathbf{u}^{mec} or ϵ_1 fields (*i.e.*, insensitive to rigid body motions). The truncation error showed that the first modes associated with \mathbf{u}^{mec} and ϵ_1 were just about three times the measurement uncertainties, which is very low given the fact that the full experimental data were reduced to one single mode.

Further, the mean crack opening displacement (MCOD) fields computed for the first mode associated with \mathbf{u}^{mec} and ϵ_1 were very close to each other and just slightly different, at small MCOD levels, for raw DIC results, which evidences the denoising effect of PCA. A two-parameter Weibull law was used to approximate the first temporal modes of the analyzed fields. Virtually the same damage duration was found for both fields, which demonstrated no influence on the characterization of the reaction kinetics by PCA. With all these observations, it is concluded that PCAs applied to \mathbf{u}^{mec} or ϵ_1 provided essentially identical trends for the modal characterization of the damage development in curing and drying of an MgO containing refractory castable.

It is important to highlight that the kinetics of curing and drying was studied using the first temporal mode, which was provided by PCA, thereby reducing the influence of user influence for crack definition. The present procedure is also less intrusive than the traditional bar resonance since no mechanical contact is needed nor ex-situ analyses.

Credit authorship statement

V.F. Sciuti: Conceptualization, Methodology, Investigation, Software, Original draft preparation, Writing - Review & Editing

R. Vargas: Conceptualization, Methodology, Investigation, Software, Original draft preparation, Writing - Review & Editing

R.B. Canto: Supervision, Conceptualization, Writing - Review & Editing, Resources, Funding acquisition, Project administration

F. Hild: Supervision, Conceptualization, Methodology, Software, Formal analysis, Writing - Review & Editing, Resources, Funding acquisition, Project administration

Declaration of conflicting interests

The author(s) declared no potential conflicts of interest with respect to the research, authorship, and/or publication of this article.

Funding

This study was financed in part by the Coordenação de Aperfeiçoamento de Pessoal de Nível Superior - Brasil (CAPES) - Finance Code 001, and the support by the PDSE grant #8881.188511/2018-01 used during the internship of VS at LMT, CAPES (Brazil) and #2018/02801-4, #2018/15266-0 and #2018/23081-0, São Paulo Research Foundation (FAPESP).

References

- Landy R. A. "Magnesia refractories". In *Refractories Handbook* edited by Charles Schacht, 109-151. Boca Raton: Mechanical Engineering-New York and Basel-Marcel Dekker Then Crc Press, 2004.
- Brandão P., Goncalves G. and Duarte A. Mechanisms of hydration/carbonation of basic refractories. *Refractories Applications* 1998; 3(3): 6–7.
- Brandão P., Goncalves G. and Duarte A. Mechanisms of hydration/carbonation of basic refractories. Pt. 2. Investigation of the kinetics of formation of brucite in fired basic bricks. *Refractories Applications* 1998; 3(2): 9–11.
- Salomão R., Bittencourt L. R. M. and Pandolfelli V. C. A novel approach for magnesia hydration assessment in refractory castables. *Ceramics International* 2007; 33(5): 803–810.
- Salomão R. and Pandolfelli V. C. The role of hydraulic binders on magnesia containing refractory castables: calcium aluminate cement and hydratable alumina. *Ceramics International* 2009; 35(8): 3117–3124.
- Silva W. M., Aneziris C. G. and Brito M. A. Effect of alumina and silica on the hydration behavior of magnesia-based refractory castables. *Journal of the American Ceramic Society* 2011; 94(12): 4218–4225.
- Souza T. M., Luz A. P., Santos T. et al. Phosphate chemical binder as an anti-hydration additive for Al_2O_3 -MgO refractory castables. *Ceramics International* 2014; 40(1): 1503–1512.
- Hild F., Bouterf A. and Roux S. Damage measurements via DIC. *International Journal of Fracture* 2015; 191(1-2): 77–105.
- Sciuti V. F., Hild F., Pandolfelli V. C. et al. Digital image correlation applied to *in situ* evaluation of surface cracks upon curing of mgo-containing refractory castables. *Journal of the European Ceramic Society* 2021; 41(1).
- Pearson K. Liii. on lines and planes of closest fit to systems of points in space. *The London, Edinburgh, and Dublin Philosophical Magazine and Journal of Science* 1901; 2(11): 559–572.
- Golub G. and Van Loan C. *Matrix Computations*. Baltimore (MD), USA: The Johns Hopkins University Press, 1983.
- Mani N. K., Haug E. J. and Atkinson K. E. Application of singular value decomposition for analysis of mechanical system dynamics. *Journal of Mechanisms, Transmissions, and Automation in Design* 1985; 107(1): 82–87.

13. Hou Z. Adaptive singular value decomposition in wavelet domain for image denoising. *Pattern Recognition* 2003; 36(8): 1747–1763.
14. Trebuňa F., Huňady R., Bobovský Z. et al. Results and experiences from the application of digital image correlation in operational modal analysis. *Acta Polytechnica Hungarica* 2013; 10(5): 159–174.
15. Jailin C. Full field modal measurement with a single standard camera. *Optics and Lasers in Engineering* 2018; 107: 265–272.
16. Grama S. N. and Subramanian S. J. Computation of full-field strains using principal component analysis. *Experimental Mechanics* 2014; 54(6): 913–933.
17. Hao W., Zhu J., Zhu Q. et al. Displacement field denoising for high-temperature digital image correlation using principal component analysis. *Mechanics of Advanced Materials and Structures* 2017; 24(10): 830–839.
18. Charbal A., Roux S., Hild F. et al. Spatiotemporal regularization for digital image correlation: Application to infrared camera frames. *Int J Num Meth Eng* 2018; 114(12): 1331–1349.
19. Passieux J. C. and Périé J. N. High resolution digital image correlation using proper generalized decomposition: PGD-DIC. *International Journal for Numerical Methods in Engineering* 2012; 92(6): 531–550.
20. Berny M., Jailin C., Bouterf A. et al. Mode-enhanced space-time dic: applications to ultra-high-speed imaging. *Measurement Science and Technology* 2018; 29(12): 125008.
21. Leclerc H., Neggers J., Mathieu F. et al. Correli 3.0, 2015. IDDN.FR.001.520008.000.S.P.2015.000.31500.
22. Sciuti V. F., Canto R. B., Neggers J. et al. On the benefits of correcting brightness and contrast in global digital image correlation: Monitoring cracks during curing and drying of a refractory castable. *Optics and Lasers in Engineering* 2020; 136: 106316.
23. Hild F. and Roux S. Digital image correlation. In Rastogi P and Hack E (eds.) *Optical Methods for Solid Mechanics. A Full-Field Approach*. Weinheim (Germany): Wiley-VCH, pp. 183–228.
24. Weibull W. A statistical theory of the strength of materials. Technical Report Report 151, Roy. Swed. Inst. Eng. Res., 1939.
25. Weibull W. A statistical distribution function of wide applicability. *ASME J Appl Mech* 1951; 18(3): 293–297.